Journal of
Materials Chemistry A

Accepted Manuscript

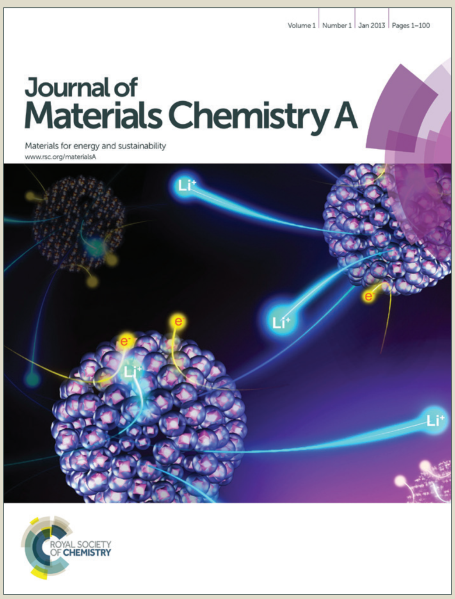

# Electronic and optical properties of mixed Sn / Pb organohalide perovskites: A first principles investigation

*Edoardo Mosconi,*[a,*] *Paolo Umari,*[b,c] *Filippo De Angelis* [a,*]

[a] Computational Laboratory for Hybrid/Organic Photovoltaics (CLHYO), CNR-ISTM, Via Elce di Sotto 8, I-06123, Perugia, Italy.

[b] Dipartimento di Fisica e Astronomia, Universita` di Padova, via Marzolo 8, I-35131 Padova, Italy,

[c] CNR-IOM DEMOCRITOS, Theory@Elettra Group, c/o Sincrotrone Trieste, Area Science Park, Basovizza, I-34012 Trieste, Italy

ABSTRACT

Organohalide lead perovskites have attracted considerable interest among emerging photovoltaic technologies, delivering highly efficient solid-state solar cells. Despite the huge potential of this class of materials, the use of Pb-containing materials will likely hamper the wide spread take off of perovskite solar cells. The development of lead-free hybrid perovskites represents thus an important step in the development of this promising technology. Very recently, the use of new mixed Pb/Sn $MASn_xPb_{(1-x)}I_3$ perovskites has been reported, with a considerable increase in the extension of the solar spectrum absorption with respect to lead-halide perovskites, shifting the absorption onset down to the near-IR. In light of the anticipated potential of Sn-based organohalide perovskites in replacing lead-based materials, here we apply a novel computational approach to the description of mixed Sn/Pb compounds showing a range of composition comparable to experimentally characterized compounds. For the investigated series of $MASn_xPb_{(1-x)}I_3$ perovskites we find a continuous and monotonic variation of the energy levels, shifting at lower potentials; and band-gaps, which shift towards the near-IR, as the Sn content in the perovskite is increased. Notably, while we find slightly unbalanced electron/hole transport in the pure phases, Pb (Sn) materials being better electron (hole) transporters, for intermediate compositions an almost perfectly balanced charge carrier transport can be achieved, in line with recent experimental observations.

## 1. Introduction

Organohalide lead perovskites have attracted considerable interest among emerging photovoltaic technologies, delivering highly efficient solid-state solar cells.[1-8] The prototype $CH_3NH_3PbI_3$ perovskite[9] ($CH_3NH_3^+$=methylammonium=MA) and the mixed halide $MAPb(I_{1-x}Br_x)_3$ [10] and $MAPb(I_{1-x}Cl_x)_3$ analogues[2, 4] have so far dominated the field. Despite the huge potential of this class of materials, the use of Pb-containing materials will likely hamper the wide spread take off of perovskite solar cells. The development of lead-free hybrid perovskites represents thus an important step in the development of this promising technology. Few investigations have been devoted up to now to the development of alternative hybrid perovskites to the most performing Pb-based ones, involving mainly analogous Sn-based compounds.[11-13] Tin is indeed a natural candidate element to replace lead, being located just above lead in the same periodic table column; organohalide tin perovskites have shown a strong optical response down to about 1000 nm, being therefore very attractive for photovoltaic applications. However, Sn(II) compounds are extremely sensitive to air,[11] possibly leading to the unwanted formation of Sn(IV) compounds, which may limit the commercialisation prospects due to stringent environmental requirements during panel manufacture and due to anticipated high costs for completely hermetic encapsulation. As a matter of fact, the state of the art efficiency for Sn-based perovskite solar cells stands at about 6%.[11-13] Very recently, the use of new mixed Pb/Sn $MASn_xPb_{(1-x)}I_3$ perovskites[14-16] for photovoltaic applications has been reported, with a considerable increase in the extension of the solar spectrum absorption with respect to lead-halide perovskites, shifting the absorption onset down to the near-IR. Promising efficiencies of 9.8 % have been reported for such compounds, leading to the consideration of their use to mitigate the Pb content in perovskite solar cell devices.[15] As mentioned by Zuo et al.,[15] however, the precise determination of the energy levels of $MASn_xPb_{(1-x)}I_3$ perovskite materials is still challenging and the reported values so far are quite scattered,[11, 13, 14, 16] potentially due to the aforementioned ease of oxidation of Sn-containing materials.

In light of the anticipated potential of Sn-based organohalide perovskites in replacing lead-based materials, considerable effort has been invested in developing a suitable computational strategy capable to accurately describe the electronic and optical properties of both Pb and Sn materials in a balanced fashion.[17-19] In this spirit, we recently developed an efficient theoretical framework[17] allowing for the accurate simulation of the electronic structure of $ASnX_3$ and $APbX_3$ perovskites rooted into a combination of DFT and GW methods including spin-orbit coupling (SOC). Here we apply this novel computational approach to the description of mixed Sn/Pb compounds showing a range of composition comparable to experimentally characterized compounds. The method of choice is a GW approach incorporating Spin Orbit Coupling (SOC),[17] see also Ref. [20] for a complementary approach, which was able to reproduce the band-gaps, absorption spectra and effective charge carrier masses for the class of metal halide perovskite, thus providing the interpretative basis for the optimal exploitation of new materials in PSCs. Several previous theoretical investigations were reported on Sn-based perovskites, mainly employing DFT methods, [21-27] but to our knowledge mixed Sn/Pb perovskites have not been addressed so far.

For the investigated series of $MASn_xPb_{(1-x)}I_3$ perovskites we find a continuous and monotonic variation of the energy levels, shifting at lower potentials; and band-gaps, which shift towards the near-IR, as the Sn content in the perovskite is increased. Notably, while we find slightly unbalanced electron/hole transport in the pure phases, Pb (Sn) materials being better electron (hole) transporters, for intermediate compositions an almost perfectly balanced charge carrier transport can be achieved, in line with recent experimental observations.[15]

## 2. Computational Details

All the calculations have been carried out without any symmetry constraint, using the PWSCF code as implemented in the Quantum-Espresso program package.[28] A tetragonal unit cell consisting of four $MASn_xPb_{(1-x)}I_3$ units was used for the investigated systems. Electron-ion interactions were described by ultrasoft pseudopotentials[29] with electrons from Pb 5d, 6s, 6p; Sn 4d, 5s, 5p; N and C

2s, 2p; H 1s; I 5s, 5p; Cs 6s, shells explicitly included in the calculations. A 4x4x4 Monkhorst–Pack grid[30] was chosen for sampling the Brillouin zone of the tetragonal and triclinic systems. Plane-wave basis set cutoffs for the smooth part of the wave functions and the augmented density of 25 and 200 Ry, respectively, were used for Scalar Relativistic (SR) DFT geometry optimizations. To check the convergence of the electronic structure calculations, we performed an 8x8x8 k-point grid SR-DFT calculation on $MAPbI_3$, finding essentially the same DOS compared to the 4x4x4 k-point grid, see Supporting Information. The PBE exchange-correlation functional was employed for all the reported calculations.[31] By following the procedure reported in our previous work,[17] SR-GW calculations were performed using norm-conserving pseudopotentials with an energy cutoff of 70 Ry defining the plane-waves used for representing the wave-functions. GW calculations including SOC[17] were performed by using ultrasoft[29] pseudopotentials and energy cut-offs of 45 and 280 for the wave-functions and charge densities, respectively. SR-GW calculations were performed developing polarizability operators on a basis sets obtained as explained in Ref. [32] using an energy cutoff of 3 Ry and selecting the 2000 most important basis vectors. The self-energy expectation values are first obtained on imaginary frequency and then analytically continued on the real frequency axis fitting with a two poles expansion.[33] SOC-GW calculations were performed including 400 Kohn-Sham states, of which the first 200 are doubly occupied. All the presented GW calculations have been performed sampling the Brillouin's zone at the Γ point only, although the starting DFT calculations and the long range parts of the dielectric matrices are evaluated using a regular 4x4x4 mesh of k-points. To calculate the band structures and DOS at the GW level we have envisaged a scheme for introducing GW corrections to DFT energy levels calculated at an arbitrary k-point considering only the GW levels calculated at the Γ-point, see Ref. [16] for further details. For evaluating the optical properties we have first evaluated the frequency dependent complex dielectric function:

$$\epsilon(\omega) = \frac{16\pi}{N_k\Omega}\sum_{\mathbf{k},v,c}\frac{\left|\left\langle\phi_{\mathbf{k}v}^{rel}\middle|\hat{\mathbf{v}}\middle|\phi_{\mathbf{k}c}^{rel}\right\rangle\right|^2}{\left(\tilde{E}_{\mathbf{k}c}^{GW}-\tilde{E}_{\mathbf{k}v}^{GW}\right)^2\left(\tilde{E}_{\mathbf{k}c}^{GW}-\tilde{E}_{\mathbf{k}v}^{GW}-\omega-i\eta\right)} \quad (1)$$

where $\Omega$ is the volume of the simulation cell, $N_k$ is the total number of k-points in the BZ, $\hat{\mathbf{v}}$ is the velocity operator, $\eta$ is an opportune broadening factor, and the indices $v$ and $c$ run over the occupied and unoccupied states, respectively. The frequency dependent absorption coefficient $\alpha(\omega)$ is then given by:

$$\alpha(\omega) = \omega\sqrt{\frac{-\mathrm{Re}\epsilon(\omega)+\sqrt{\mathrm{Re}^2\epsilon(\omega)+\mathrm{Im}^2\epsilon(\omega)}}{2}} \qquad (2)$$

**3. Results and discussion**

To simulate the mixed $MASn_xPb_{(1-x)}I_3$ perovskites we chose to gradually reduce the percentage of Pb in the starting (quasi) I4cm tetragonal system found for $MAPbI_3$ (x = 0).[34,35] To ensure a continuous variation in the investigated properties we employed the same tetragonal cell made by four MASn/$PbI_3$ units for all calculations. We used both experimental cell parameters (when available) and optimized atomic and cell parameters along the entire series of compounds obtained moving towards the $MASnI_3$ perovskite (x = 1).

Both pure Pb- and Sn-based perovskites were studied in our previous work.[17] For $MAPbI_3$ we further optimized the MA cation position in a recently published paper[35] obtaining a further stabilization of 0.12 eV (structure 1 in ref. [35]) with respect to structure reported in Ref. [17]. Although many different structures, originated by a different arrangement of the MA cations, are calculated to lie within less than 0.1 eV, calling for a dynamical sampling of the investigated properties, here we just use the most stable structure found within the investigated data set.[35] We further applied the same starting MA orientation reported for structure 1 in ref. [35] for the entire mixed Sn/Pb perovskites series. Notably, also for $MASnI_3$ perovskites we obtained a 0.09 eV of stabilization with respect to $MASnI_3$ reported in ref.[17] . We will thus mainly refer to the data corresponding to the most stable structures found in this paper.

Recent calculations demonstrated that inclusion of van der Waals interactions delivered calculated cell parameters of $MAPbI_3$ in better agreement with experimental values.[36-39] When accounting for dispersion interactions in our computational set-up, the calculated cell parameters for various arrangements of the MA cations in $MAPbI_3$ decreased, as expected, but neither the relative stability order nor the main structural features, e.g. the *c/a* ratio, were affected. Similarly, the calculated band-gaps all decreased by ca. 0.1 eV, by virtue of the volume contraction, but their trends remained unchanged.[35] Notably, by increasing the plane waves expansion cut-off the cell parameters decreased, thus here we take advantage of some cancellation of errors due to the two effects.

The simulated unit cell contains four $MASn/PbI_3$ units, so we can naturally simulate three values of the Pb:Sn ratio, namely 3:1 (x = 0.25), 2:2 (x = 0.50) and 1:3 (x = 0.75) in addition to the pure phases of each material (x=0 and 1). While for the species with x =0.25 and x = 0.75 the position of the minority metal atom is irrelevant (all sites being roughly equivalent), for the system corresponding to x = 0.50 we need to replace two metals and we consequently have more than one option for the relative position of the two Pb and Sn atoms in the unit cell. In this case, we thus explored the three possible structural arrangements for x = 0.50 named A, B and C in Figure 1. Structure A shows the Sn and Pb atoms alternated along the 110 and 001 crystallographic directions, while structures B and C show the presence of two consecutive Pb / Sn atoms along the 001 and 110 direction, respectively.

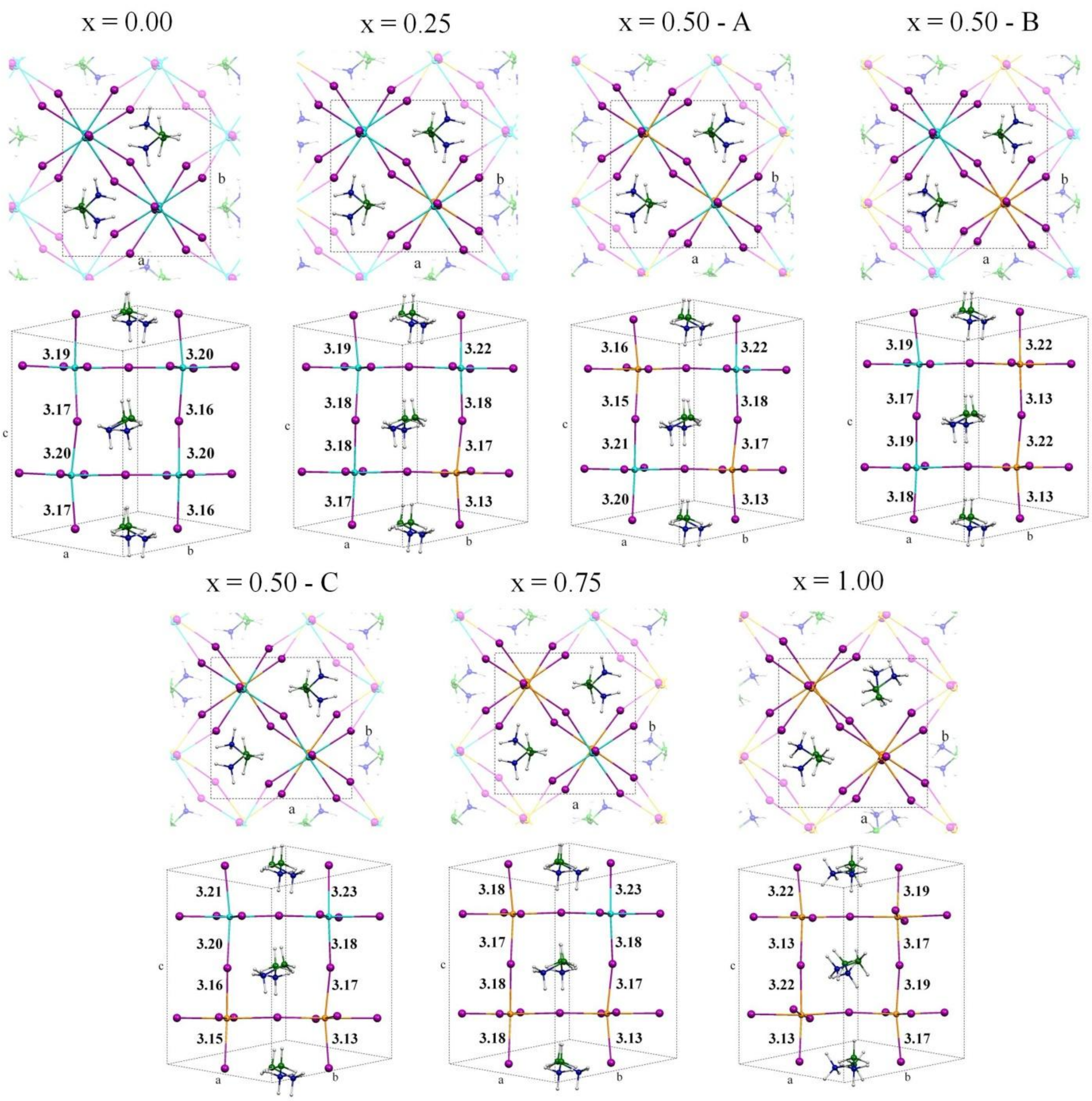


**Figure 1.** Optimized structures and main geometrical parameters for the investigated $MASn_xPb_{(1-x)}I_3$ series. For x=0.25 and x=0.75 only one of the four equivalent structures is reported, while for x=0.50 the three inequivalent structures are reported labeled as A, B and C, se text for definitions. Pb= light blue; Sn= orange; I= purple; N= blue; C= green, H= white.

Geometry optimizations of the investigated $MASn_xPb_{(1-x)}I_3$ compounds have been carried out at the SR-DFT level considering the $MAPbI_3$ experimental cell parameters,[40] see structure in Figure 1, and by performing a variable cell relaxation, see optimized cell parameters in Table 1. Moreover, for the pure Sn-based perovskite also we performed a geometry optimization using the $MASnI_3$ tetragonal I4cm β-phase experimental cell reported in Ref. [12]. By performing a variable cell relaxation, we found a slight decrease of the volume with increasing the Sn percentage (maximum contraction of 3.3 % for the pure Sn-based perovskite compared to the pure Pb-based species). This is in good agreement with X-Ray measured data[16] which showed only minimal differences between the mixed $MASn_xPb_{(1-x)}I_3$ species with respect to the pure $MAPbI_3$ material. Interestingly, the three different configurations explored for x = 0.50 show essentially the same stability, with calculated energy differences within less than 0.01 eV. This suggests that there is no preferential tendency to create separate $MAPbI_3$ and $MASnI_3$ domains in the mixed metal perovskite materials but rather a perfect miscibility is expected. For all subsequent investigations we will refer to the A mixed system with x= 0.5, which corresponds to the fully mixed phase.

**Table 1**. Optimized cell parameters (Å) and cell volume (Å$^3$) for the investigated mixed $MASn_xPb_{(1-x)}I_3$ perovskites.

| | Sn fraction (x) | | | | |
|---|---|---|---|---|---|
| Lattice parameters | 0.00 | 0.25 | 0.50 | 0.75 | 1.00 |
| a | 8.751 | 8.742 | 8.735 | 8.710 | 8.681 |
| b | 8.735 | 8.723 | 8.722 | 8.697 | 8.670 |
| c | 12.770 | 12.745 | 12.678 | 12.657 | 12.535 |
| Vol | 976.139 | 971.889 | 965.895 | 958.779 | 943.438 |
| ΔVol. % | 0.0 | -0.4 | -1.0 | -1.8 | -3.3 |

To gain insight into the electronic and optical properties of the investigated series of compounds, we performed additional DFT and GW calculations (both SR and SOC) on the optimized geometries, the results are shown in Table 2. In particular, in line with what previously found for the pure Sn- and Pb-based perovskites,[17] for the mixed Sn/Pb materials, SR-DFT and SR-GW deliver an unbalanced description of the band-gap series going from x = 0.00 to 1.00, while both SOC-GW and SOC-DFT reproduce the experimental decreasing of the band gap. Notably, as previously found,[17] only SOC-GW calculations are able to quantitatively (within ± 0.2 eV) reproduce the experimental band-gaps of the investigated materials, see Table 2, with SOC-DFT delivering considerable underestimates. We predict a steady decrease of the band-gap upon increasing the Sn content in the perovskite, which is in line with the results by Ogomi et al.,[16] while a slight band-gap increase for the pure Sn-based perovskite was reported by Hao et al.[14] For each composition, a reduced band gap is calculated when employing calculated atomic and cell parameters, in line with recent results pointing at a band-gap reduction upon cell compression.[27]

**Table 2**. Band gap (eV) calculated at different levels of theory for the investigated $MASn_xPb_{(1-x)}I_3$ mixed perovskites. The first entry corresponds to data calculated on optimized geometries employing the experimental cell parameters of MAPbI3. The second entry (in parentheses) refers to optimized atomic and cell parameters. For pure MASnI3, values denoted with * are calculated at the experimental $MASnI_3$ cell parameters.

| | Sn fraction (x) | | | | |
|---|---|---|---|---|---|
| | 0.00 | 0.25 | 0.50 | 0.75 | 1.00 |
| SR-DFT | 1.57 (1.47) | 1.27 (1.11) | 1.14 (0.95) | 0.86 (0.66) | 0.66/0.54* (0.43) |
| SR-GW | 2.66 (2.52) | 2.31 (2.17) | 2.15 (2.04) | 1.82 (1.69) | 1.66/1.55* (1.42) |
| SOC-DFT | 0.53 (0.53) | 0.39 (0.34) | 0.43 (0.33) | 0.34 (0.23) | 0.39/0.25* (0.21) |
| SOC-GW | 1.64 (1.66) | 1.37 (1.31) | 1.41 (1.24) | 1.20 (1.06) | 1.31/1.00* (0.89) |
| Exp.[a] | 1.51 | 1.31 | 1.28 | 1.23 | 1.10 |
| Exp.[b] | 1.55 | 1.24 | 1.17 | 1.17 | 1.30 |

[a] from Ref. [16]; [b] from Ref. [14];.

To analyze the optical properties of the Sn/Pb mixed perovskites, we simulated the SOC-GW absorption spectra for the series of $MASn_xPb_{(1-x)}I_3$, see Figure 2. As expected from the behavior of the calculated band gap, we found a red shift of the simulated absorption onset by increasing the Sn percentage, in agreement with the experimental measurements.[16] Also interesting, is the increased absorption coefficient found by increasing the Sn content in the perovskite, which makes Sn-based materials extremely interesting alternatives to replaces fully Pb-based materials. Notably, the calculated absorption coefficient of $MASnI_3$ is in good agreement with the experimental data (ca. $2x10^4$ $cm^{-1}$ in the band-gap region) reported by Noel et al.[11]

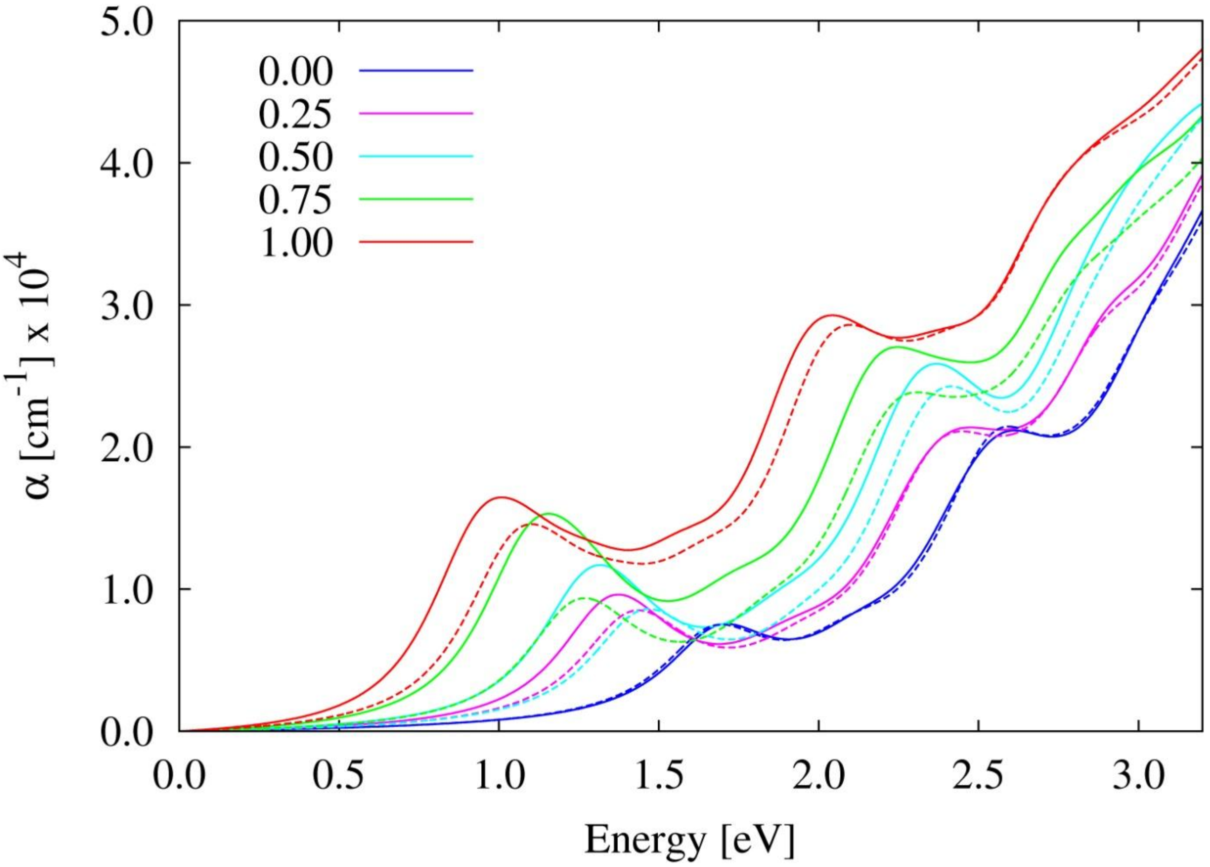


**Figure 2.** Simulated SOC-GW absorption spectra for the $MASn_xPb_{(1-x)}I_3$ series of perovskites. Solid lines are referred to the optimized atomic and cell parameters; dashed lines for x from 0.00 to 0.75 are referred to $MAPbI_3$ experimental cell parameters and for x = 1.00 are referred to the experimental $MASnI_3$ cell parameters.

To evaluate the HOMO and LUMO energy levels of the mixed metal perovskites and compare them the VB and CB shift of the mixed metal halide perovskites with respect to the experimental measurements, we aligned the calculated SOC-GW Densities of States (DOS) to the MA carbon atoms levels, see Figure 3. This alignment strategy was shown to be a reasonable approximation to align the levels of Pb and Sn compounds,[17] since it is expected that the methyl moieties of the MA cations will only weakly interact with the inorganic cavity, thus showing a reduced variability in the Pb or Sn environments. In line with the band-gap variation, the DOS evolution by varying x from 0 to 1 is smooth and continuous, with a marked rise of the VB edge and a less pronounced rise of the VB edge, leading to the observed band-gap reduction by increasing the Sn content into the perovskite.

Notably, the shape of the DOS close to the VB/CB edges also varies, with increasing Sn content introducing strongly hybridized Sn *5s* states at the VB top, see Figure 4, as previously noted for $MASnI_3$, leading to reduced hole effective masses.[17] Interestingly, for x=0.5, i.e. for an equal amount of Sn and Pb, the CB structure still shows the characteristic shape which is typical of $MAPbI_3$, associated to decreased electron effective masses, while for x=0.75 the CB resembles that of the pure $MASnI_3$ compound.

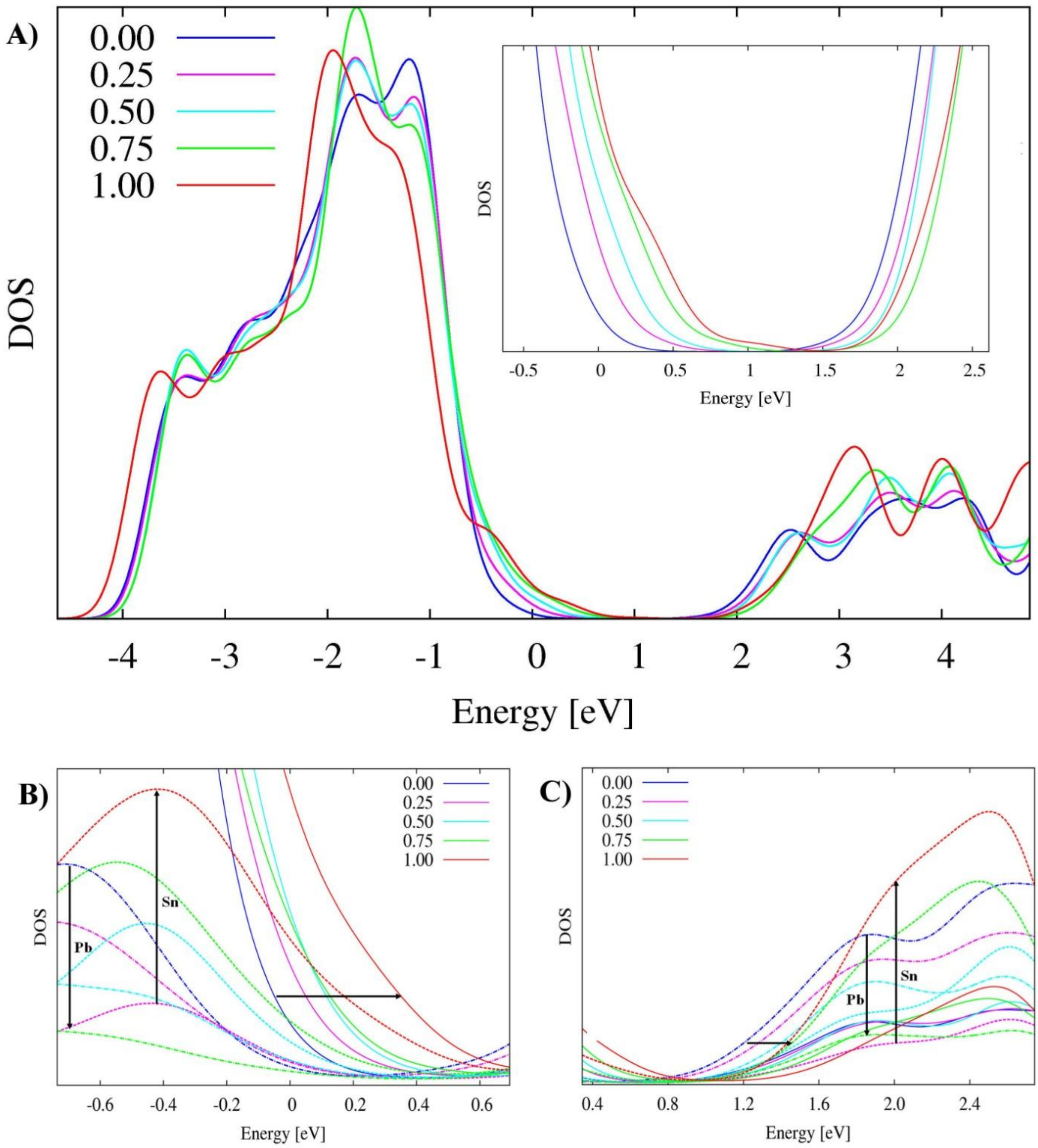


**Figure 3**. A) DOS calculated at SOC-GW method for $MASn_xPb_{(1-x)}I_3$ by moving form x = 0 to x = 1.00. Values for x from 0.00 to 0.75 are referred to geometry with $MAPbI_3$ experimental cell and for x = 1.00 are referred to the $MASnI_3$ cell parameters. B) and C) SOC-DFT DOS calculated for the investigated series showing contributions from the Pb/Sn atoms /dashed lines) and I atoms (solid lines).

A marked difference in the experimental studies by Ogomi et al. and Hao et al. was found in the evolution of the VB and CB positions by varying the relative Sn/Pb ratio. While Ogomi et al. predicted a steady variation of the VB and CB edges by increasing the Sn content,[16] resulting in an energy upshift of both levels, Hao et al.[14] reported a totally different trend with a non monotonic variation of the energy levels. We report in Table 3 the calculated HOMO and LUMO energy shifts (setting the corresponding data for x=0 to 0 energy) calculated by SOC-GW (see Supporting Information for different levels of theory) while a graphical of the calculated aligned SOC-GW energy levels is compared to the experimental data by Ogomi et al.[16] in Figure 4. The SOC-GW calculated energy levels in Table 3 and Figure 4 clearly show that by increasing the Sn percentage we predict an steady up-shift of the VB which is only partially compensated by the reduced CB up-shift. This result is in good agreement with the experimental measurements reported by Ogomi et al. [16] as demonstrated by plotting experimental level shifts vs. calculated ones with slope ~ 1, see Figure S1 in Supporting Information. To check that the calculated trend in energy levels is not due to the different phase (P4mm vs I4cm) reported by Hao et. al, we simulated the pure P4mm $MASnI_3$ perovskite and we compared the calculated SR-DFT DOS with the corresponding one for the I4cm structure. By doing so, we find an additional up-shift of the CB level of 0.12 eV for the P4mm phase, see Supplementary Information, indicating that the difference between theory and experiment is not due to the different considered phases.

**Table 3.** HOMO and LUMO energy levels shifts (eV) by varying the Sn/Pb ratio calculated at the SOC-GW level and compared to the experimental measurements.[16] VB and CB shifts evaluated from the SOC-GW DOS are also reported. Energy shifts are referred to the pure $MAPbI_3$ perovskites (set as zero). VB and CB values are calculated at 1.4 % of the maximum VB peak of the $MAPbI_3$ calculated SOC-GW DOS. Values in parentheses are referred to the optimized atomic and cell parameters.

| | Sn content | | | | |
|---|---|---|---|---|---|
| | 0.00 | 0.25 | 0.5 | 0.75 | 1.00 |
| | | | Exp. | | |
| $\Delta E^{HOMO}$ | 0.00 | 0.27 | 0.44 | 0.47 | 0.66 |
| $\Delta E^{LUMO}$ | 0.00 | 0.07 | 0.21 | 0.19 | 0.25 |
| $Gap^{EXP}$ | 1.51 | 1.31 | 1.28 | 1.23 | 1.10 |
| | | | SOC-GW | | |
| $\Delta E^{HOMO}$ | 0.00 (0.00) | 0.34 (0.35) | 0.46 (0.65) | 0.76 (0.93) | 0.99 (1.11) |
| $\Delta E^{LUMO}$ | 0.00 (0.00) | 0.08 (0.00) | 0.23 (0.23) | 0.32 (0.32) | 0.35 (0.33) |
| $Gap^{H-L}$ | 1.64 (1.66) | 1.37 (1.31) | 1.41 (1.24) | 1.20 (1.06) | 1.00 (0.89) |
| $\Delta E^{VB}$ | 0.00 (0.00) | 0.20 (0.20) | 0.35 (0.43) | 0.53 (0.50) | 0.64 (0.68) |
| $\Delta E^{CB}$ | 0.00 (0.00) | 0.08 (0.10) | 0.17 (0.19) | 0.27 (0.20) | 0.19 (0.18) |
| $Gap^{VB-CB}$ | 1.74 (1.87) | 1.62 (1.77) | 1.56 (1.63) | 1.48 (1.57) | 1.29 (1.37) |

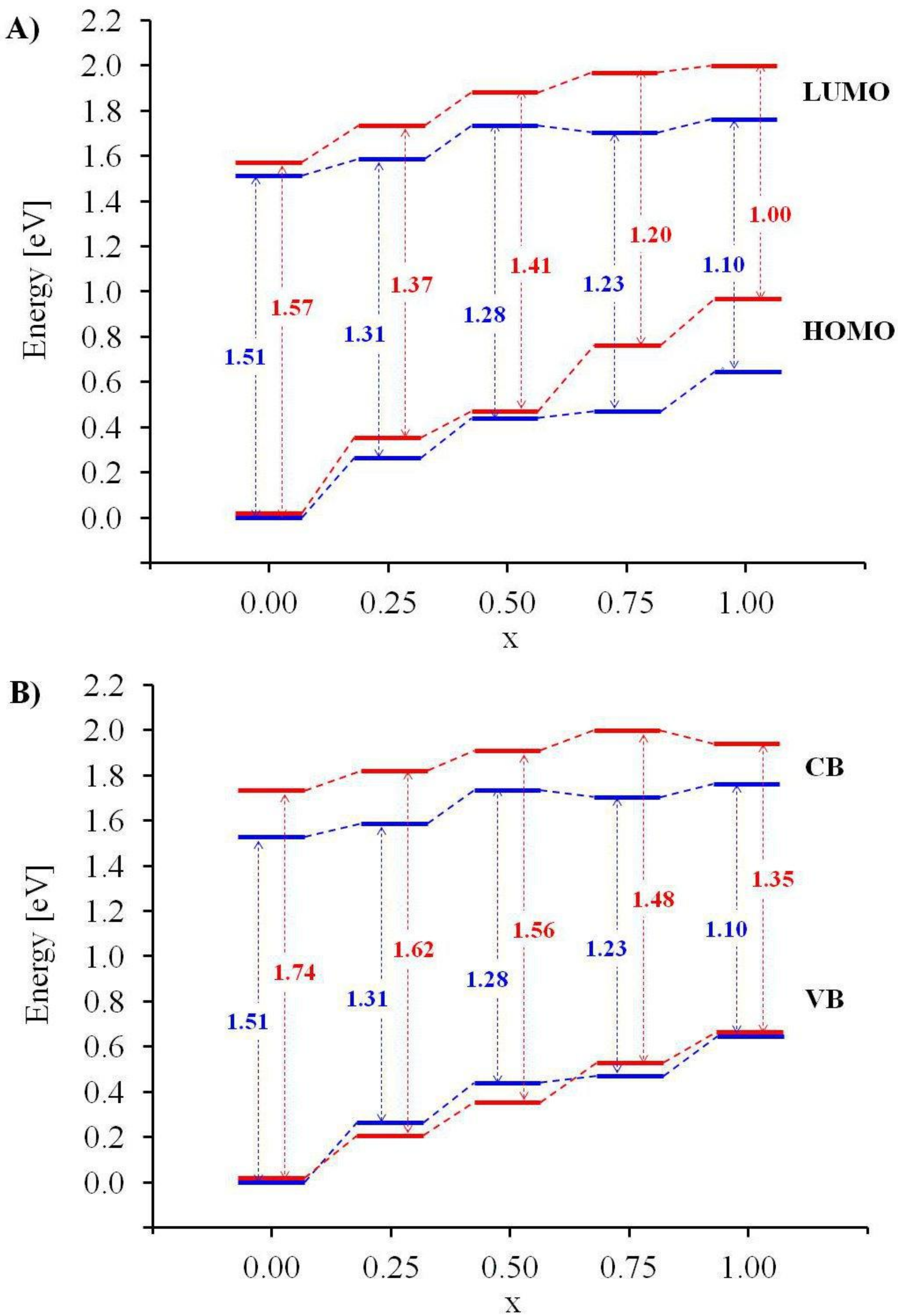


**Figure 4.** Energy levels alignment of the calculated SOC-GW HOMO/LUMO (A) and VB/CB (B) (in red) compared with the experimental values (in blue). [16] Values for x from 0.00 to 0.75 are

referred to geometry with $MAPbI_3$ experimental cell; values for x = 1.00 are referred to the $MASnI_3$ cell parameters. VB and CB values are calculated at 1.4 % of the maximum VB peak of the $MAPbI_3$ calculated SOC-GW DOS.

To gain insight into the transport properties of the investigated $MASn_xPb_{(1-x)}I_3$ perovskites, we calculated the effective carrier masses for the entire series by means of parabolic band fitting around the band gap (Γ point of the Brillouin zone). The results, shown in Figure 5, show a gradual inversion of the average of the electron end hole masses going from x = 0.00 to x = 1.00. While for the pure Pb-base material we found electron mass smaller than the hole mass for the Sn-based perovskite we found electron mass greater than the hole mass; the intermediate mixed Sn/Pb systems shows and intermediate and balanced electron and hole masses values. Notice, that as previously reported, the lack of inversion symmetry in the calculated quasi I4cm unit cell, to the effect of SOC, leads to a k-dependent band splitting (Rashba/Dresselhaus effect),[17, 35, 41-43] which also slightly varies by decreasing the Pb content in the mixed perovskites, see Supporting Information.

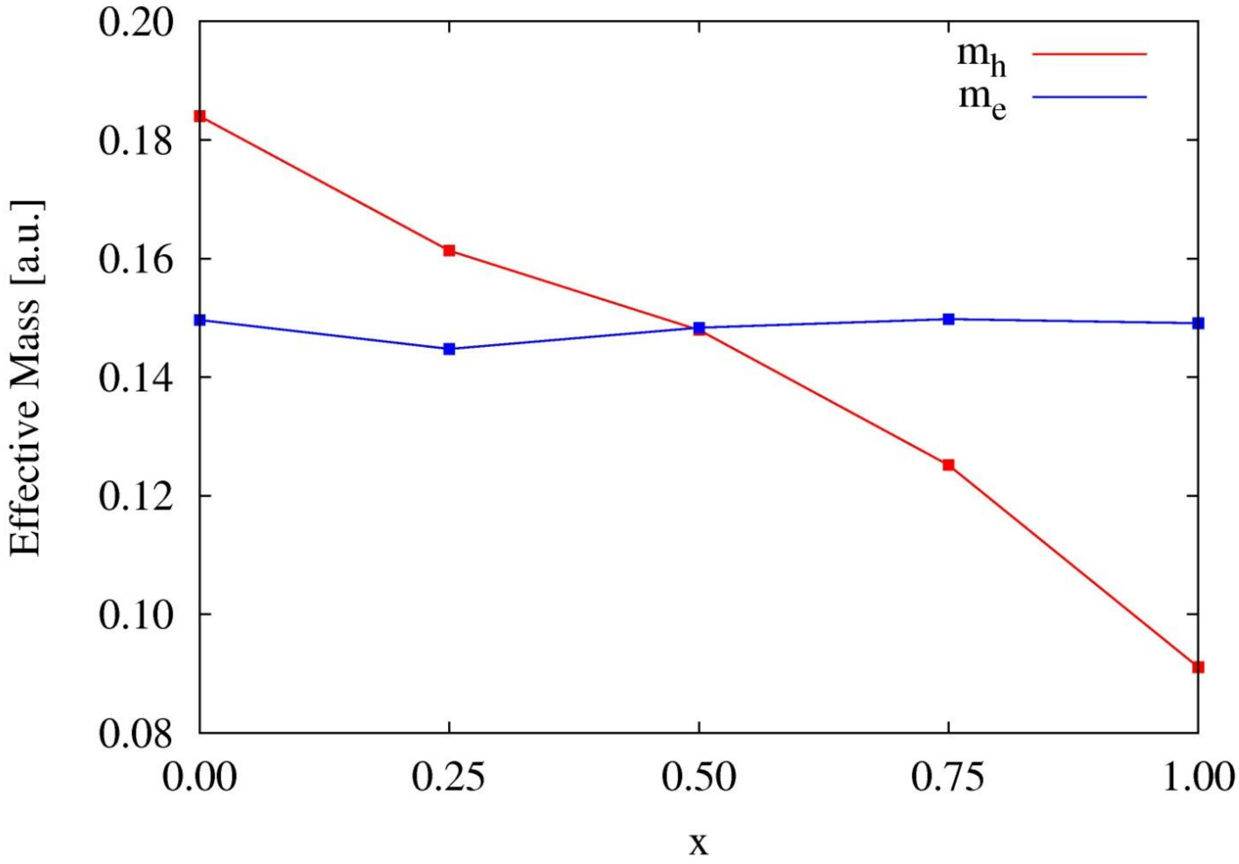


**Figure 5**. Calculated SOC-DFT effective hole and electron masses for the mixed Sn/Pb perovskites.

## 4. Conclusions

In summary, we have investigated by first principles computational techniques the series of mixed Pb/Sn perovskites of type $MASn_xPb_{(1-x)}I_3$ by moving form x = 0 to x = 1.00. Our results showed a steady and monotonic variation of the optical absorption spectra, energy levels and transport properties when moving along the series. In line with previous reports, a red-shifted absorption and increased optical absorption is found for the pure $MASnI_3$ compared to analogous $MAPbI_3$, which is also retrieved when increasing the investigated mixed perovskites. While $MASnI_3$ is predicted to be a better hole transporter, $MAPbI_3$ is predicted to be a better electron transporter. Notably, by varying the Sn/Pb content, we demonstrate that the 50:50 compound retains the best of each compound, showing a red-shifted and increased absorption spectra along with an almost perfectly balanced electron and hole transport properties, as derived by the calculated effective masses. At the same time, while above this Sn/Pb ratio, the material oxidation could become significant, the 50:50 compound seems to be sufficient stable to oxidation, as measured by a HOMO energy more positive than 5 eV vs. vacuum.

While the search for totally Pb-free materials still remains a major topic in perovskite solar cells, our study shows that the 50:50 mixed Pb/Sn perovskite could represent a winning compound to mitigate the Pb content in the perovskites while showing possibly increased performances compared to the prototype $MAPbI_3$ material.

**Acknowledgment.** The research leading to these results has received funding from the European Union Seventh Framework Programme [FP7/2007%2013] under grant agreement n° 604032 of the MESO project.

**Electronic Supplementary Material.** Additional Figures and Tables.

**References.**

1. Zhou, H.; Chen, Q.; Li, G.; Luo, S.; Song, T.-b.; Duan, H.-S.; Hong, Z.; You, J.; Liu, Y.; Yang, Y. Interface engineering of highly efficient perovskite solar cells. *Science* **2014,** 345, 542-546.
2. Lee, M. M.; Teuscher, J.; Miyasaka, T.; Murakami, T. N.; Snaith, H. J. Efficient Hybrid Solar Cells Based on Meso-Superstructured Organometal Halide Perovskites. *Science* **2012,** 338, 643-647.
3. Kim, H.-S.; Lee, C.-R.; Im, J.-H.; Lee, K.-B.; Moehl, T.; Marchioro, A.; Moon, S.-J.; Humphry-Baker, R.; Yum, J.-H.; Moser, J. E., et al. Lead Iodide Perovskite Sensitized All-Solid-State Submicron Thin Film Mesoscopic Solar Cell with Efficiency Exceeding 9%. *Sci. Rep.* **2012,** 2.
4. Liu, M.; Johnston, M. B.; Snaith, H. J. Efficient planar heterojunction perovskite solar cells by vapour deposition. *Nature* **2013,** 501, 395-398.
5. Burschka, J.; Pellet, N.; Moon, S.-J.; Humphry-Baker, R.; Gao, P.; Nazeeruddin, M. K.; Gratzel, M. Sequential deposition as a route to high-performance perovskite-sensitized solar cells. *Nature* **2013,** 499, 316-319.
6. Jeon, N. J.; Noh, J. H.; Kim, Y. C.; Yang, W. S.; Ryu, S.; Seok, S. I. Solvent engineering for high-performance inorganic–organic hybrid perovskite solar cells. *Nat. Mater.* **2014,** 13, 897-903.
7. Jung, H. S.; Park, N.-G. Perovskite Solar Cells: From Materials to Devices. *Small* **2014**, DOI: 10.1002/smll.201402767.
8. Bai, Y.; Mora-Seró, I.; De Angelis, F.; Bisquert, J.; Wang, P. Titanium Dioxide Nanomaterials for Photovoltaic Applications. *Chemical Reviews* **2014,** 114, 10095-10130.
9. Baikie, T.; Fang, Y.; Kadro, J. M.; Schreyer, M.; Wei, F.; Mhaisalkar, S. G.; Grätzel, M.; White, T. J. Synthesis and crystal chemistry of the hybrid perovskite $(CH_3NH_3)PbI_3$ for solid-state sensitised solar cell applications. *J. Mater. Chem. A* **2013,** 1, 5628-5641.
10. Noh, J. H.; Im, S. H.; Heo, J. H.; Mandal, T. N.; Seok, S. I. Chemical Management for Colorful, Efficient, and Stable Inorganic–Organic Hybrid Nanostructured Solar Cells. *Nano Lett.* **2013,** 13, 1764-1769.
11. Noel, N. K.; Stranks, S. D.; Abate, A.; Wehrenfennig, C.; Guarnera, S.; Haghighirad, A.-A.; Sadhanala, A.; Eperon, G. E.; Pathak, S. K.; Johnston, M. B., et al. Lead-free organic-inorganic tin halide perovskites for photovoltaic applications. *Energy Environ. Sci.* **2014,** 7, 3061-3068.

12. Stoumpos, C. C.; Malliakas, C. D.; Kanatzidis, M. G. Semiconducting Tin and Lead Iodide Perovskites with Organic Cations: Phase Transitions, High Mobilities, and Near-Infrared Photoluminescent Properties. *Inorg. Chem.* **2013,** 52, 9019-9038.
13. Hao, F.; Stoumpos, C. C.; Cao, D. H.; Chang, R. P. H.; Kanatzidis, M. G. Lead-free solid-state organic-inorganic halide perovskite solar cells. *Nat Photon* **2014,** 8, 489-494.
14. Hao, F.; Stoumpos, C. C.; Chang, R. P. H.; Kanatzidis, M. G. Anomalous Band Gap Behavior in Mixed Sn and Pb Perovskites Enables Broadening of Absorption Spectrum in Solar Cells. *J. Am. Chem. Soc.* **2014,** 136, 8094-8099.
15. Zuo, F.; Williams, S. T.; Liang, P.-W.; Chueh, C.-C.; Liao, C.-Y.; Jen, A. K. Y. Binary-Metal Perovskites Toward High-Performance Planar-Heterojunction Hybrid Solar Cells. *Adv. Mater.* **2014**, DOI: 10.1002/adma.201401641.
16. Ogomi, Y.; Morita, A.; Tsukamoto, S.; Saitho, T.; Fujikawa, N.; Shen, Q.; Toyoda, T.; Yoshino, K.; Pandey, S. S.; Ma, T., et al. CH3NH3SnxPb(1–x)I3 Perovskite Solar Cells Covering up to 1060 nm. *J. Phys. Chem. Lett.* **2014,** 5, 1004-1011.
17. Umari, P.; Mosconi, E.; De Angelis, F. Relativistic GW calculations on $CH_3NH_3PbI_3$ and $CH_3NH_3SnI_3$ Perovskites for Solar Cell Applications. *Sci. Rep.* **2014,** 4, 4467.
18. De Angelis, F. Modeling Materials and Processes in Hybrid/Organic Photovoltaics: From Dye-Sensitized to Perovskite Solar Cells. *Acc. Chem. Res.* **2014**, DOI: 10.1021/ar500089n.
19. Yin, W.-J.; Yang, J.-H.; Kang, J.; Yan, Y.; Wei, S.-H. Halide perovskite materials for solar cells: a theoretical review. *J. Mater. Chem. A* **2015**.
20. Brivio, F.; Butler, K. T.; Walsh, A.; van Schilfgaarde, M. Relativistic quasiparticle self-consistent electronic structure of hybrid halide perovskite photovoltaic absorbers. *Phys. Rev. B* **2014,** 89, 155204.
21. Borriello, I.; Cantele, G.; Ninno, D. Ab initio investigation of hybrid organic-inorganic perovskites based on tin halides. *Phys. Rev. B* **2008,** 77, 235214.
22. Takahashi, Y.; Obara, R.; Lin, Z.-Z.; Takahashi, Y.; Naito, T.; Inabe, T.; Ishibashi, S.; Terakura, K. Charge-transport in tin-iodide perovskite $CH_3NH_3SnI_3$: origin of high conductivity. *Dalton Trans.* **2011,** 40, 5563-5568.
23. Chiarella, F.; Zappettini, A.; Licci, F.; Borriello, I.; Cantele, G.; Ninno, D.; Cassinese, A.; Vaglio, R. Combined experimental and theoretical investigation of optical, structural, and electronic properties of $CH_3NH_3SnX_3$ thin films (X=Cl,Br). *Phys. Rev. B* **2008,** 77, 045129.
24. Chung, I.; Song, J.-H.; Im, J.; Androulakis, J.; Malliakas, C. D.; Li, H.; Freeman, A. J.; Kenney, J. T.; Kanatzidis, M. G. $CsSnI_3$: Semiconductor or Metal? High Electrical Conductivity and Strong Near-Infrared Photoluminescence from a Single Material. High Hole Mobility and Phase-Transitions. *J. Am. Chem. Soc.* **2012,** 134, 8579-8587.
25. Feng, J. Mechanical properties of hybrid organic-inorganic CH3NH3BX3 (B = Sn, Pb; X = Br, I) perovskites for solar cell absorbers. *APL Mater.* **2014,** 2, -.
26. Feng, J.; Xiao, B. Effective Masses and Electronic and Optical Properties of Nontoxic MASnX3 (X = Cl, Br, and I) Perovskite Structures as Solar Cell Absorber: A Theoretical Study Using HSE06. *J. Phys. Chem. C* **2014,** 118, 19655-19660.
27. Castelli, I. E.; García-Lastra, J. M.; Thygesen, K. S.; Jacobsen, K. W. Bandgap calculations and trends of organometal halide perovskites. *APL Mater.* **2014,** 2.
28. Giannozzi, P.; Baroni, S.; Bonini, N.; Calandra, M.; Car, R.; Cavazzoni, C.; Ceresoli, D.; Guido, L. C.; Cococcioni, M.; Dabo, I., et al. QUANTUM ESPRESSO: a modular and open-source software project for quantum simulations of materials. *J. Phys.: Condens. Matter* **2009,** 21, 395502.
29. Vanderbilt, D. Soft self-consistent pseudopotentials in a generalized eigenvalue formalism. *Phys. Rev. B* **1990,** 41, 7892-7895.
30. Monkhorst, H. J.; Pack, J. D. Special points for Brillouin-zone integrations. *Phys. Rev. B* **1976,** 13, 5188-5192.
31. Perdew, J. P.; Burke, K.; Ernzerhof, M. Generalized Gradient Approximation Made Simple. *Phys. Rev. Lett.* **1996,** 77, 3865-3868.
32. Umari, P.; Stenuit, G.; Baroni, S. GW quasiparticle spectra from occupied states only. *Phys. Rev. B* **2010,** 81, 115104.
33. Rieger, M. M.; Steinbeck, L.; White, I. D.; Rojas, H. N.; Godby, R. W. The GW space-time method for the self-energy of large systems. *Comp. Phys. Comm.* **1999,** 117, 211-228.

34. Stoumpos, C. C.; Malliakas, C. D.; Kanatzidis, M. G. Semiconducting Tin and Lead Iodide Perovskites with Organic Cations: Phase Transitions, High Mobilities, and Near-Infrared Photoluminescent Properties. *Inorg. Chem.* **2013,** 52, 9019−9038.
35. Quarti, C.; Mosconi, E.; De Angelis, F. Interplay of Orientational Order and Electronic Structure in Methylammonium Lead Iodide: Implications for Solar Cell Operation. *Chem. Mater.* **2014,** 10.1021/cm5032046.
36. Egger, D. A.; Kronik, L. Role of Dispersive Interactions in Determining Structural Properties of Organic-Inorganic Halide Perovskites: Insight from First-Principle Calculations. *J. Phys. Chem. Lett.* **2014,** 5, 2728-2733.
37. Wang, Y.; Gould, T.; Dobson, J. F.; Zhang, H.; Yang, H.; Yao, X.; Zhao, H. Density functional theory analysis of structural and electronic properties of orthorhombic perovskite CH3NH3PbI3. *Phys. Chem. Chem. Phys.* **2014,** 16, 1424-1429.
38. Menéndez-Proupin, E.; Palacios, P.; Wahnón, P.; Conesa, J. C. Self-consistent relativistic band structure of the $CH_3NH_3PbI_3$ perovskite. *Phys. Rev. B* **2014,** 90, 045207.
39. Szczęśniak, M. M.; Brenstein, R. J.; Cybulski, S. M.; Scheiner, S. Potential energy surface for dispersion interaction in water dimer and hydrogen fluoride dimer. *J. Phys. Chem.* **1990,** 94, 1781-1788.
40. Poglitsch, A.; Weber, D. Dynamic disorder in methylammoniumtrihalogenoplumbates (II) observed by millimeter-wave spectroscopy. *J. Chem. Phys.* **1987,** 87, 6373-6378.
41. Even, J.; Pedesseau, L.; Jancu, J.-M.; Katan, C. DFT and k · p modelling of the phase transitions of lead and tin halide perovskites for photovoltaic cells. *Phys. Status Solidi Rapid Res. Lett.* **2014,** 8, 31-35.
42. Kim, M.; Im, J.; Freeman, A. J.; Ihm, J.; Jin, H. Switchable S = 1/2 and J = 1/2 Rashba bands in ferroelectric halide perovskites. *Proc. Natl. Acad. Sci.* **2014,** 111, 6900-6904.
43. Amat, A.; Mosconi, E.; Ronca, E.; Quarti, C.; Umari, P.; Nazeeruddin, M. K.; Grätzel, M.; De Angelis, F. Cation-Induced Band-Gap Tuning in Organohalide Perovskites: Interplay of Spin–Orbit Coupling and Octahedra Tilting. *Nano Lett.* **2014,** 14, 3608-3616.

## Table of contents entry.

We investigate $MASn_xPb_{(1-x)}I_3$ perovskites by first-principles simulations, finding monotonic variation of energy levels and band-gaps, and demonstrating balanced electron/hole transport.